Check for updates

View Article Online
View Journal

Chemical
Science

Accepted Manuscript

This article can be cited before page numbers have been issued, to do this please use: G. Ma, Z. Ju, Y. Chen, R. Wang, Z. Yuan, H. Du, M. Cai, M. Gao, Y. Wang and G. Yu, *Chem. Sci.*, 2025, DOI: 10.1039/D5SC00311C.

ROYAL SOCIETY
OF CHEMISTRY

rsc.li/chemical-science

View Article Online
DOI: 10.1039/D5SC00311C

High-capacity organic cathode boosted by coordination chemistry for energy-dense aqueous zinc-organic batteries

Received 00th January 20xx,
Accepted 00th January 20xx

DOI: 10.1039/x0xx00000x

Guanzhong Ma[1,†], Zhengyu Ju[2,†], Yutong Chen[1], Runmo Wang[1], Zihao Yuan[1], Huiping Du[1], Mian Cai[1] , Meng Gao[1], Yaqun Wang[1,*], and Guihua Yu[2, *]

N-type organic cathode materials containing carbonyl and imine groups have emerged as promising candidates for zinc-ion batteries due to their excellent charge storage capability, which arise from the synergic storage of both Zn^{2+} and H^+. However, an increase in active sites also complicates synthesis, introduces complex multi-electron reactions, and hinders a comprehensive understanding of the charge storage mechanism and the evolution of molecular configuration during electrochemical process. Herein, a 10-electron transfer organic cathode material, featuring imine and quinone groups spaced apart, was synthesized in one-step. Its highly conjugated molecular structure promotes electron delocalization, thereby enhancing stability. The competitive storage mechanism of Zn^{2+} and H^+ was unveiled through multiple *quasi-situ* spectroscopy techniques and calculations, revealing that Zn^{2+} are initially coordinated to form O-Zn-N, followed by the co-insertion of H^+/Zn^{2+} during the reduction of the carbonyl groups. Thanks to Zn^{2+}/H^+ co-insertion and coordination stabilization, an ultra-high capacity of 445 mAh g^{-1} at a current density of 0.2 A g^{-1} and a retained capacity of 200 mAh g^{-1} (>80% capacity retention) at 10 A g^{-1} after 15,000 cycles can be achieved. The molecular structure-related charge storage mechanism revealed in this study can provide useful design considerations for realizing high-capacity, fast-charging and long-duration organic cathodes for various energy storage systems.

Introduction:

With the growing research on aqueous zinc-ion batteries (AZIBs), the design of cathode materials has emerged as a key factor determining the high performance of these batteries[1-3]. Organic materials, such as stable organic radicals[4], conductive polymers[5], triphenylamine[6], dinitrobenzene[7], and phenothiazine[8], significant improvements in charging and discharging performance have been observed when these are used as cathodes[9-11]. Among various organic cathode materials for AZIBs, imine (C=N) and carbonyl (C=O) organics have garnered significant interests owing to their unique molecular structure characterized by stability and designability[12-14]. Carbonyl compounds are widely used in AZIBs due to their high theoretical specific capacity and ease with which can be modified by chemical and physical methods[15,16]. However, some carbonyl compounds are unstable in aqueous environments and tend to dissolve, resulting in instability[17]. Imine compounds offer notable advantages as cathodes in AZIBs, including higher activity during charging and discharging, which suggests faster reaction kinetics[18,19]. However, unmodified imine compounds often exhibit lower discharge voltages when employed as cathodes in AZIBs[20,21]. Moreover, repeated charging and discharging cycles can lead to structure changes, highlighting the need for improved electrochemical stability[22,23].

The Integration of these two functional groups into a single compound appears to effectively address these challenges[24,25]. In recent years, cathode materials featuring C=O and C=N bonds as dual active sites for energy storage in AZIBs have been widely reported. For example, Shi et al[26]. reported an four electrons organic cathode material, benzo[b]phenazine-6,11-dione (BPD), which exhibited a discharge specific capacity of up to 429 mAh/g in a 2 M $ZnSO_4$ aqueous electrolyte (at a current density of 0.05 A/g). Song's team introduced a six electrons cathode material, 5,7,12,14-tetraaza-6,13-pentacenequinone (TAPQ), which demonstrated a discharge specific capacity of up to 443 mAh/g[27]. Chen et al[28]. carefully considered the binding effects of C=O and C=N on zinc ions and designed a twelve electrons material with a triangular planar structure, hexaazatrinaphthalene-quinone (HATNQ), which exhibited strong electrochemical stability. To improve material stability and ion transport capability, Peng et al[29]. designed a cathode material with dual active units, dipyrido[3’,2’:5,6;2”,3”:7,8]quinoxalino[2,3-i]dipyrido[3,2-a:2’,3’-c]phenazine-10,21-dione (DQDPD), through a strategy of expanding the π-conjugation of N-heterocycles. The synergistic effect of these two functional groups enhances the discharge specific capacity of ZIBs and improves their interfacial chemical stability. Consequently, designing and synthesizing electrode materials with a high density of active units is a crucial approach to improving the electrochemical performance of ZIBs[30,31]. One key strategy involves maximizing the number of active sites per molecule to enhance the theoretical specific capacity of electrode material. However, as the number of active sites increase, it becomes increasingly challenging to synthesize the materials in a straightforward manner. Furthermore, while many reports have partially explored the molecular design of C=O and C=N-based compounds, a clear understanding of the insertion mechanisms of Zn^{2+} and H^+ when both functional groups coexist in a single molecule remain elusive[32].

In this work, the reaction of 2,3-diaminonaphthalene-1,4-dione (DANQ) and 2,3,5,6-tetrachlorocyclohexa-2,5-diene-1,4-dione (TCBQ) was conducted via a facile one-pot method, synthesizing an 10-electron organic compound named 6,8,15,17-tetrahydrobenzo[b]benzo[6,7] quinoxalino[2,3-i]phenazine-5,7,9,14,16,18-hexaone (TBQPH). The synthetic compound consists of six p-benzoquinone structures connected by four imine groups, supplying sufficient coordination sites for the H^+/Zn^{2+} in the electrochemical reaction. As the positive electrode material for

---

[a] College of Energy Storage Technology, Shandong University of Science and Technology, Qingdao 266590, China.
[b] Materials Science and Engineering Program and Walker Department of Mechanical Engineering, The University of Texas at Austin, TX, 78712, USA.

† These authors contributed equally to this work.

Electronic Supplementary Information (ESI) available: [details of any supplementary information available should be included here]. See DOI: 10.1039/x0xx00000x

View Article Online
DOI: 10.1039/D5SC00311C

aqueous ZIBs in 1 M zinc sulphate ($ZnSO_4$) electrolyte, the TBQPH@GO electrode demonstrated an extraordinary capacity of 445 mAh g^{-1} at a current density of 0.2 A g^{-1}. Even under a high current density of 10 A g^{-1}, a high capacity of 200 mAh g^{-1} could be retained. Moreover, a remarkable capacity retention of ~80% after extensive cycling for 15,000 cycles could be achieved. Such high-capacity retention could be attributed to the insoluble property of the molecule as validated by in situ ultraviolet (UV) spectroscopy. Furthermore, the charge storage mechanism of TBQPH was systematically investigated using quasi situ X-ray photoelectron spectroscopy (XPS) and Fourier transform infrared spectroscopy (FTIR) techniques. A H^+/Zn^{2+} co-insertion mechanism was revealed TBQPH in 1 M $ZnSO_4$ electrolyte. In addition, the reaction order of H^+/Zn^{2+} ion was unveiled via electrochemical analysis and theoretical calculations. To sustain the charge storage mechanism of the TBQPH, Fukui function (FUKUI) calculations were performed, showing the preferential central carbonyl group as the reactive cites in the molecule. Density functional theory (DFT) calculations were also conducted to calculate Gibbs free energy (ΔG) for the redox reaction, verifying that the first reduction platform is contributed by Zn^{2+} coordination while subsequent platforms are attributed to the co-insertion of Zn^{2+} and H^+ which leads to a 10-electron transfer reaction in TBQPH@GO. This organic electrode based on TBQPH@GO offer enhanced capacity and stability for ZIB towards increased performance and practicality.

Results and Discussion:

Here, we designed a straightforward synthetic procedure for TBQPH, a planar organic molecule with conjugated carbonyl and imine groups, via the ammonolysis reaction between DANQ and TCBQ (Figure 1A). By comparison, it was found that fully conjugated TBQPH with super-electronic off-domain has a smaller gap (E_g) (1.186 eV) between LUMO and HOMO, which gives it a higher conductivity for fast electron transfer and rapid redox kinetics (Figure 1B). The decrease in the energy gap can be correlated to the high degree of electron conjugation and electron delocalization in the TBQPH, which is further supported by its Localized orbital locator profiles (Figure 1E).[33] Through the ^1H and ^{13}C nuclear magnetic resonance (NMR) spectroscopy, the successful synthesis of TBQPH was verified (Figure 1F, *SI Appendix,* Figure S2). The chemical structure of the TBQPH was characterized by the FTIR (*SI Appendix,* Figure S3). The prominent peaks located at the wavelengths of ~1700 and ~1250 cm^{-1} can be attributed to the bending vibration of C=O and C–N bonds, respectively, in the units of TBQPH. The presence of C=O and C–N functional groups was further identified by the XPS (Figure 1C and D). In the N 1s spectra, the peaks located at 399 and 402 eV correspond to the N–H and C–N bonding, respectively (Figure 1C). Notably, in the C 1s spectra, besides the C–C, C=C, C–N and C=O peaks apparently from the molecular structure of the TBQPH, a distinct π-π stacked structure at 289 eV can also be observed (Figure 1D). Such π-π interaction can be attributed to stacking of planar TBQPH molecules, as characterized through the transmission electron microscopy (TEM) (Figure 1G and H). Layered features can be observed in the TEM image (Figure 1G) and the interval between the molecular planes can be measured to be ~0.32 nm (Figure 1H). Irregular powdery structure with the micrometer particle size can be seen from the scanning electron microscopy (SEM) due to the severe π-π stacking of the TBQPH molecule (*SI Appendix,* Figure S1). The uniform element distribution of C, N and O can be clearly seen via the EDS surface mapping (Figure 1I), and the atomic ratio (C-O-N) is calculated to be 13:3:2 which is close to the ideal elemental ratio of the TBQPH (*SI Appendix,* Figure S4).

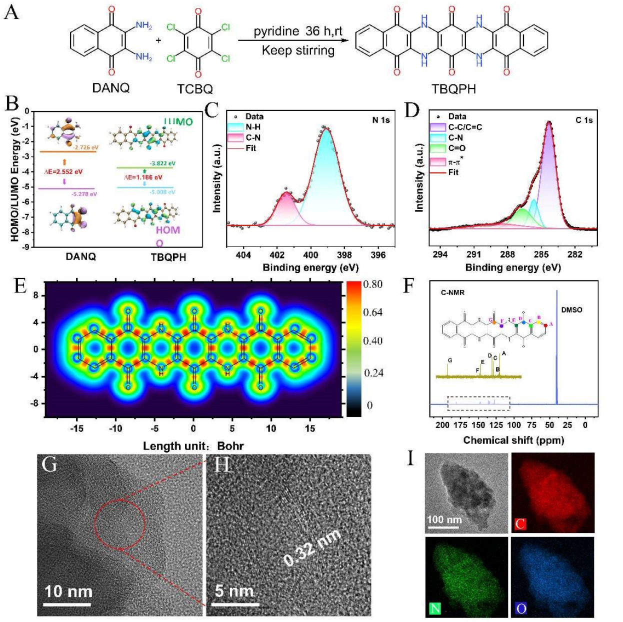

Figure. 1. Synthesis and structural characterizations of the TBQPH. **A**, one-step synthesis procedure of TBQPH via the ammonolysis reaction. **B**, DFT-calculated LUMO/HOMO energy levels of TADQ and TBQPH. **C,D,** XPS spectra of N 1s (**C**) and C 1s (**D**) of TBQPH, respectively. **E**, Colour-filled diagram of the molecular fixed-domain orbitals of TBQPH. **F**, NMR images of TBQPH material: H atomic spectrum. **G,H**, TEM images of TBQPH.**I**, TEM image and corresponding EDS mapping of C , N , and O in TBQPH, respectively.

For the ideal cathode materials, it is crucial to possess exceptional electrical conductivity, high reactivity, and remarkable stability. [34,35] The reactivity and stability of the material can be directly related to its particle size and stacked structure. To fully exploit the material's reactivity and enhance its stability, graphene oxide (GO) was incorporated into the synthetic process through an in situ method, resulting in the formation of TBQPH@GO (Figure 2A). The TBQPH nanoparticles grown in situ on GO exhibit no discernible structural changes induced by the substrate, as evidenced by a clear comparison of their FTIR and Raman spectra. Notably, TBQPH and TBQPH@GO exhibit nearly identical FTIR signals (Figure 2B), while the presence of D-peak and the G-peak of GO weakens the intensity of Raman peaks for these materials (Figure 2C). The XPS spectra demonstrate the consistency of the active unit material (Figure 2D and E). It is noteworthy that TBQPH@GO exhibits a stronger π-π structure, attributed to the properties of GO rather than materials stacking or crystallization (Figure 2D). This can be distinctly observed in SEM images (Figure 2F), where smaller TBQPH particles grow on the surface of GO, resulting in improved dispersion and a larger

View Article Online
DOI: 10.1039/D5SC00311C

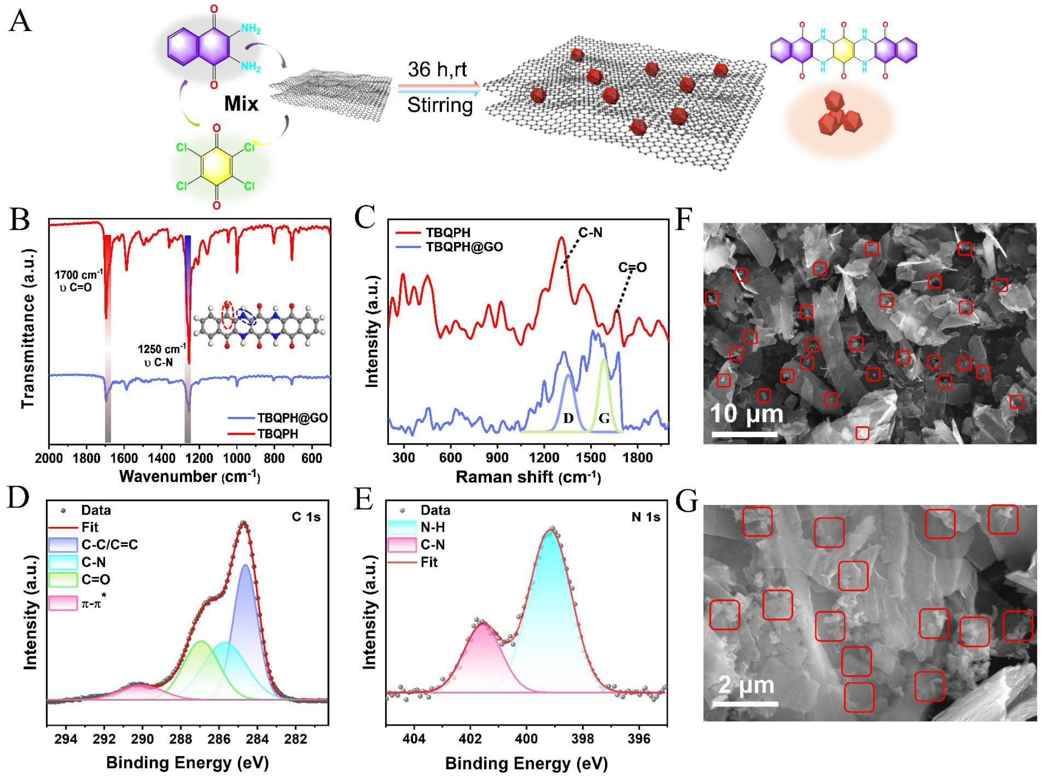

Figure. 2. Synthesis and structural characterizations of the TBQPH@GO. **A,** *in situ* synthetic procedure of TBQPH@GO. **B,** FTIR spectra of TBQPH and TBQPH@GO. **C,** Raman spectra of TBQPH and TBQPH@GO. **D,E,** XPS spectra of C 1s (**D**) and N 1s (**E**) of TBQPH@GO. **F,G,** SEM images of TBQPH@GO at different magnifications.

contact area for ionic interaction, thereby facilitating the activity of TBQPH. The XRD analysis reveals that the dispersion of the sample on GO enhances the π-π stacking interaction (*SI Appendix,* Figure S5). Additionally, the exceptional electrochemical stability of GO significantly enhances the stability of TBQPH in electrolytes.

The reaction mechanism of conjugated structures containing both carbonyl and imine groups has not been well understood in the previous studies.[36,37] Due to the polyionic nature of the aqueous electrolyte (containing both H^+ and Zn^{2+}), competition between H^+ and Zn^{2+} occurs at the electrodes, resulting in a distinct order of charge storage in n-type organic materials. It is often hypothesized that the smaller H^+ ions are more likely to approach the reaction active sites, while the coordinated N-Zn-O structure with enhanced stability leads to reduced energy levels upon electron acquisition. To elucidate the reaction mechanism of TBQPH, combined electrochemical characterizations and DFT calculations were conducted. Electrostatic potential (ESP) method was employed to speculate the electrophilic and nucleophilic reaction-active sites to get insights into the active sites.[38] In Figure 3A, the red region represents the positive ESP value (electrophilic center) and blue region stands for the negative ESP value (nucleophilic center). The sites with more negative ESP areas prefer electrophilic reactions, which are considered highly reactive sites. During the initial discharge, all the capacity can be attributed to the carbonyl group due to the presence of the hydrogen atom on the imine group (Figure 3A). Figure 3B shows a typical CV curve of the TBQPH@GO electrode in the first cycle. Upon the first discharge, two reduction peaks at 0.55 and 0.80 V can be observed, indicating the reaction between carbonyl groups and Zn^{2+}/H^+ ions. Subsequently, during the charging process, in addition to the two oxidation peaks at 0.78 and 1.15 V, which correspond to the two reduction peaks in the discharge process, a third oxidation peaks at 1.19 V appears (Figure 3B), which represents the removal of the hydrogen atoms from the imine groups in the TBQPH. Consequently, the electrostatic configuration surrounding the N atoms within the material molecule transitions to a lower state, indicating its oxidized state (Figure 3A).

The charge storage mechanism of the TBQPH can be unveiled via *quasi-situ* XPS measurements, wherein the data points collected at different voltages at the first charge-discharge cycle are shown in Figure 3C. It is worth noting that the shift of the XPS peaks arises from the electron gain and loss and the change of electron cloud density surrounding the redox material during the reaction. During the discharge of TBQPH, electrons accumulate on the material, increasing the electron cloud density and shifting the XPS peak towards lower binding energy. Conversely, when TBQPH is charged, electrons are depleted, reducing the electron cloud density and shifting the XPS peak towards higher binding energy. As seen from the O 1s spectra, the binding of O atoms on the carbonyl groups with Zn^{2+} and H^+ can be clearly observed as the formation of C–O–Zn and C–O–H bonds in the initial discharge (Figure 3D). However, there is no significant change as N atoms do not participate in this process (Figure 3E). During the charging process of TBQPH, C–O–Zn and C–O–H bonds disappear while C=O bonds reform. Additionally, –NH– groups are oxidized to –N= at the fully charged state (Figure 3D and

View Article Online
DOI: 10.1039/D5SC00311C

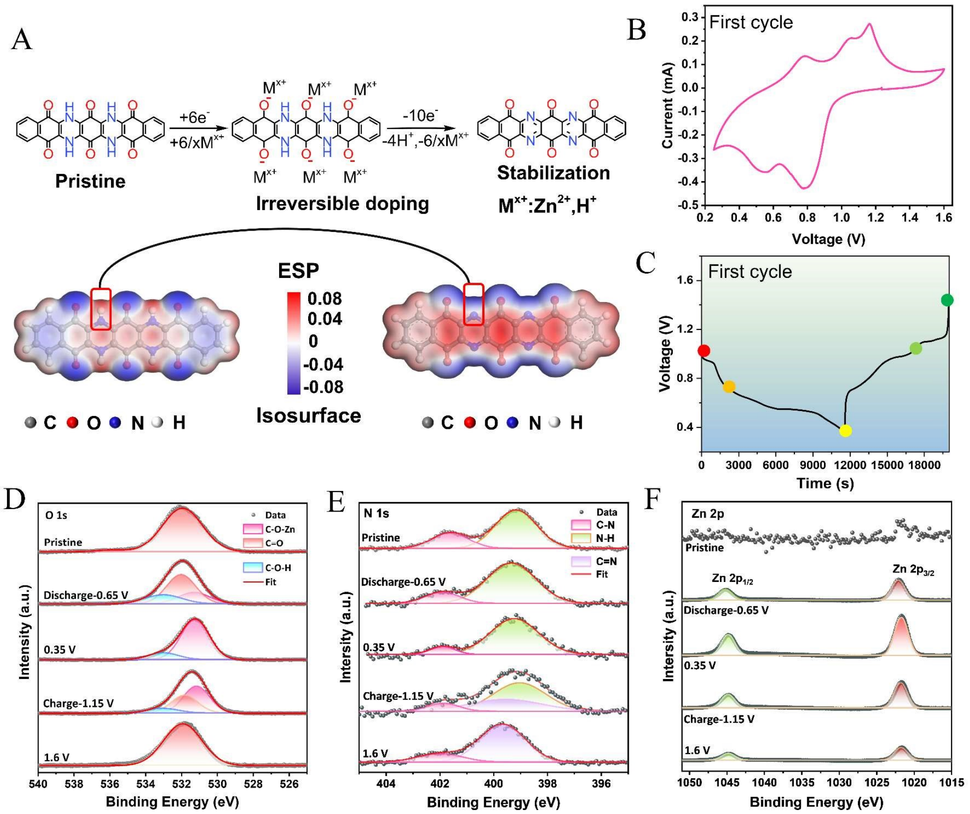

Figure. 3. Charge storage mechanism of the TBQPH during stabilization with *quasi-situ* electrochemical and structural characterizations. **A**, Electrochemical redox reaction of the TBQPH at the first cycle, with DFT-calculated electrostatic distributions of the pristine and stabilized states of TBQPH. **B**, CV profile of TBQPH@GO. **C**, GCD profile of TBQPH@GO. **D-F**, *quasi-situ* XPS spectra of O 1s (**D**), N 1s (**E**), and Zn 2p (**F**) of TBQPH@GO at the first charge-discharge cycle.

E). Furthermore, the change of Zn^{2+} states during charge and discharge process was investigated (Figure 3F). The intensity of Zn 2p peaks are enhanced upon discharge and weakened upon charge, indicating the insertion and removal of Zn^{2+} within the material. The slight peaks observed in the initial state originate from the electrolyte. In addition, the C 1s spectra clearly reveals the evolution of the active functional groups at different charge and discharge states (*SI Appendix*, Figure S6). As the discharge proceeds, the C=O bond proportion decreases and disappears, which is then restored upon charging. Moreover, C=N bond does not form in the discharge process, but gradually appears during the charging process, which is well aligned with the conclusion from the N 1s spectra. Through the electrochemical and structural analysis of the TBQPH at the first charge-discharge cycle, the charge storage mechanism, that is, the 6-electron discharge to the reduced state and 10-electron charge process to the stabilized oxidized state, can be clearly presented.

The charge storage mechanism of TBQPH was further thoroughly investigated to gain a comprehensive understanding of the subsequent redox processes after its stabilization. The Fukui function (FUKUI) calculations (*SI Appendix*, Figure S7 and Table S1) were conducted on the oxidized state of TBQPH to analyze the specific reactive sites where nucleophilic attack first take place in the reduction process. The FUKUI calculation results reveal that the carbonyl oxygen atoms at the central position have the maximum f^+ value, which have the highest reactivity with the electron acquisition preference. The significant difference between the first and second cycles can be observed in the CV curves (Figure 4A and 3B). It is noted that three pairs of redox peaks can be observed at 0.50/0.78 V, 0.62/1.15 V and 0.85/1.19 V in the 2nd to 4th cycles (*SI Appendix*, Figure S8). In addition, the GCD profiles of these cycles demonstrated that TBQPH was oxidized to a stable molecular configuration with three redox plateaus after the first cycle. Changes in ion concentration in the $ZnSO_4$ electrolyte affect the magnitude of the response current but do not influence the material's primary reaction (*SI Appendix*, Figure S9). To minimize the impact of excessively high or low electrolyte concentrations on battery performance (such as the formation of basic zinc sulfate at high zinc ion concentrations), 1 M $ZnSO_4$ electrolyte was chosen as the primary test concentration.

To figure out whether the first reduction peak R1 is attributed to Zn^{2+} insertion, we conducted CV tests on the TBQPH@GO/Zn cell using a proton-free deep eutectic electrolyte of butanedinitrile and zinc perchlorate (*SI Appendix*, Figure S10). The reduction peak at ~0.8 V agrees with the insertion behavior observed in a 1M $ZnSO_4$ electrolyte, implying that the R1 is related to Zn^{2+} insertion. Furthermore, the charge-discharge tests were conducted on the TBQPH@GO/Zn cells in different electrolyte systems to investigate the insertion order of Zn^{2+} and H^+ (Figure 4B). It is evident that a

View Article Online
DOI: 10.1039/D5SC00311C

consistent discharge plateau (approximately 0.95-1 V) can be observed in the 1M $ZnSO_4$ electrolyte and the deep eutectic electrolyte of nitrile butanedic acid and zinc perchlorate, further validating Zn^{2+} insertion mechanism in this reduction process. However, in the H_2SO_4 electrolyte (pH = 1M $ZnSO_4$), the plateau for R1 disappears and obvious plateaus of R2 and R3 at low potentials can be observed, indicating that H^+ insertion is not related to the R1 process but involves into the R2 and R3 processes. GITT profile of the TBQPH@GO//Zn cell (*SI Appendix*, Figure S11) reveals a large IR compensation for the plateau at high potentials, which is probably because the embedding of Zn^{2+} is more difficult compared to H^+, verifying that the first R1 plateau of the discharge belongs to the embedding of Zn^{2+}.

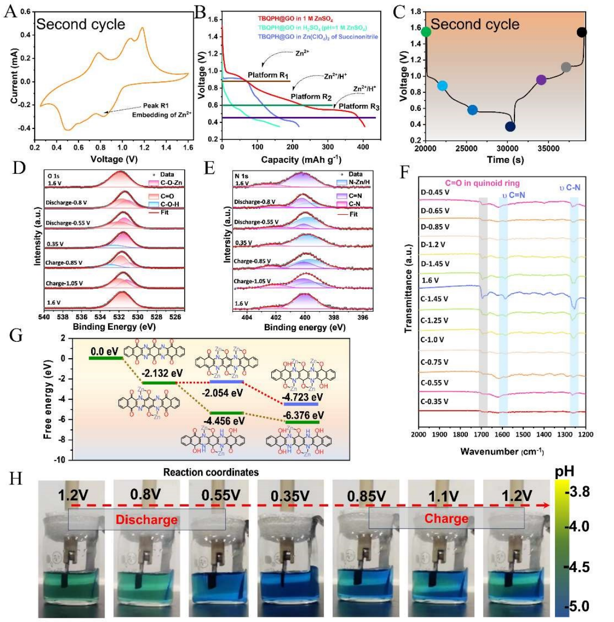

Figure. 4. Charge storage mechanism of the TBQPH after stabilization with *quasi-situ* electrochemical and structural characterizations. **A**, CV profiles of TBQPH@GO at the second cycle. **B**, Galvanostatic discharge curves of TBQPH@GO//Zn cells in different electrolytes. **C**, GCD profile of TBQPH@GO. **D**,**E**, *quasi-situ* XPS spectra of O 1s (**D**) and N 1s (**E**) of TBQPH@GO at the second charge-discharge cycle. **F**, *quasi-situ* FTIR spectra of TBQPH@GO at different voltages. **G**, DFT calculations of Gibbs free energy of TBQPH for the insertion of Zn^{2+} and H^+. **H**, Images showing pH change with the indicator during charge-discharge cycles in a TBQPH@GO//Zn cell.

The *quasi-situ* XPS measurements of the stabilized TBQPH structure provide further understanding of the insertion mechanisms of Zn^{2+} and H^+. The XPS spectra were collected at different voltages at the second charge-discharge cycle (Figure 4C). As seen in the O 1s spectra, it is evident that Zn^{2+} initially binds to the carbonyl group by the formation of C–O–Zn, followed by the H^+ insertion forming C–O–H with the carbonyl group as the discharge process proceeds (Figure 4D). Notably, the insertion potential of H^+ is generally lower than that of Zn^{2+}, consistent with the distinct plateaus observed using different electrolytes. For the N 1s spectra in Figure 4E, when discharged to 0.8 V, the peak generated at the lower binding energy can be attributed to the formation of N-Zn as H^+ will not participate in the reduction process above this potential, as seen in the discharge voltage profiles with the H_2SO_4 electrolyte (Figure 4C). In the further discharge process to 0.35 V, the increase of the peak can be attributed to the insertion of H^+, as the peaks of N-Zn and N–H cannot be clearly separated here. The C 1s spectra exhibit decreased C=N and C=O peaks in the discharge process which agrees with the molecular evolution from the stabilized state to the reduced state (*SI Appendix*, Figure S12). The Zn 2p spectra also show an increased Zn peak during discharge as the Zn^{2+} insertion reaction proceeds. In the *quasi-situ* FTIR spectra, as the cell undergoes discharge, a decrease of C=O and C=N peaks can be observed, attributed to their reduction into C–O and C–N species (Figure 4F). Intriguingly, a decline in the C–N peak is also observed with decreasing potentials; however, the peak position shifts to a higher wavenumber. Such peak shift is probably due to the N-Zn coordination along with Zn^{2+} insertion which serves to stabilize the structure and dampen C–N vibrations.

Theoretical calculations were further conducted to reveal the charge storage mechanism during the redox process. To analyze the Gibbs free energies associated with different ions inserted at each stage, we conducted DFT calculations on the potential insertion order of Zn^{2+} and H^+ in TBQPH. As shown in Figure 4G, consistent with the FUKUI function prediction, the carbonyl groups at the center prefer to coordinate two Zn^{2+} along with the adjacent imine groups. The Gibbs free energy associated with Zn^{2+} binding to the neighboring carbonyl group were also calculated to see if more Zn^{2+} can be inserted. However, insertion of another two Zn^{2+} is not possible as such molecular configuration exhibits a higher free energy of -2.05 eV compared to that of the insertion of four H^+ (-4.46 eV). In addition, we considered the co-storage of Zn between two TBQPH molecules and showed that C=O and C=N co-bound a Zn^{2+} with the lowest energy (-4.56), suggesting a high synergistic effect of C=O and C=N on Zn^{2+} (*SI Appendix*, Figure S13). The subsequent insertion of H^+ appears to enhance the molecular stability which is consistent with the experimental results where H^+ insertion occurs at low potentials.

With the integration of experimental characterization and calculations, we can draw the conclusion that the TBQPH preferentially induces the insertion of Zn^{2+}, resulting in the formation of a stabilized N-Zn-O coordinated structure, followed by the co-insertion of Zn^{2+} and H^+. The pH changes in the electrolyte caused by H^+ insertion into TBQPH@GO was further visualized by introducing a bromocresol green indicator into the electrolyte (Figure 4H). The indicator exhibited pale green as the pH of 1M $ZnSO_4$ was ~4.0. As the discharge reached the second plateau, the electrolyte color near the TBQPH@GO electrode turned to blue indicating an increase in pH. This color alteration can be attributed to H^+ insertion and manifested as a blue-to-green transition near the positive electrode during the charging process. However, no discernible change in color occurred near the negative electrode due to the inevitable hydrogen precipitation reaction on the Zn metal negative electrode, resulting in an elevation of surrounding electrolyte pH. The change in zinc sulfate base can be monitored from the in-situ XRD data (SI Appendix, Figure S14). This change is more pronounced when discharged to low potentials, indicating that the intercalation of H^+ predominantly occurs at low potentials, which is consistent with the previous test results.

The reaction kinetics of TBQPH@GO was investigated using CV at various sweep rates ranging from 0.2 to 1.0 mV s^{-1}. As shown in Figure 5A, the three pairs of redox peaks of TBAPH@GO exhibit slight shifts with increasing sweep rates, indicating the excellent charge

View Article Online
DOI: 10.1039/D5SC00311C

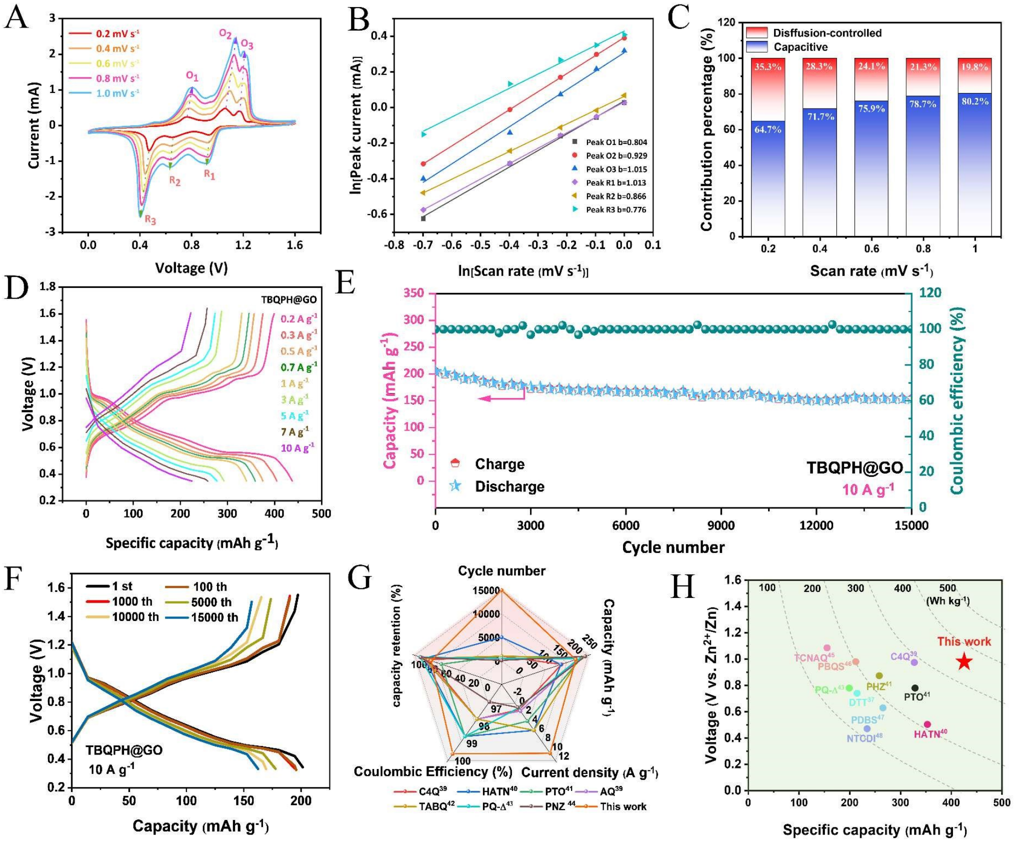

Figure. 5. Electrochemical properties of the TBQPH@GO//Zn batteries. **A,** CV profiles of the TBQPH@GO at varying sweep rates. **B,** Plot of ln(*i*) versus ln(*v*) for redox peaks. **C,** Capacity contribution of the TBQPH@GO at different sweep rates. **D,** Rate capabilities of the TBQPH@GO//Zn battery at current densities from 0.2 to 10 A g^{-1}. **E,F,** Long-term cycling performance (**E**) and corresponding charge-discharge voltage profiles (**F**) of the TBQPH@GO//Zn battery at a current density of 10 A g^{-1}. **G,** Performance comparation of the TBQPH@GO//Zn battery with other state-of-the-art zinc-organic batteries. **H,** Comparison of the TBQPH with other state-of-the-art organic cathode materials in terms of specific capacity, operating voltage, and energy density.

transfer kinetics of TBAPH@GO. According to the relationship between the peak current (*i*) and the sweep rate (*v*) in the formula $i = av^b$, *b* values (O1-3 and R1-3) are of 0.804, 0.929, 1.015, 1.013, 0.866 and 0.766 for the six redox peaks, respectively (Figure 5B). The value of *b* equals 1 indicating a surface-controlled process while equals 0.5 suggesting a diffusion-controlled process for the charge storage. The high *b* values of the TBAPH@GO indicate the redox processes are more capacitive with rapid charge storage kinetics. The proportions of each process are further evaluated via the equation $i = k_1v + k_2v^{1/2}$, wherein the surface-controlled capacity accounts for 64.7% at 0.2 mV s^{-1} and increases to 80.2% when the sweep rate increases to 1.0 mV s^{-1}, indicating that the surface-controlled process dominates throughout reaction process (Figure 5C and *SI Appendix*, Figure S15). The impedance spectroscopy measurements of the TBQPH@GO//Zn cell under different voltages reveal that the charge transfer resistance decreases during discharge, indicating the enhanced off-domain transport property and mobility of electrons inside the highly conjugated molecular structure (*SI Appendix*, Figure S16).

The electrochemical performance of the TBAPH@GO//Zn batteries was further investigated under different current densities. An ultra-high discharged capacity of 445 mAh g^{-1} can be achieved at a current density of 0.2 A g^{-1} and a retained capacity of 230 mAh g^{-1} can be delivered at a high current density of 10 A g^{-1} (Figure 5D). It is noted that the high capacity and fast kinetics of the TBAPH@GO are also related to the decreased particle size and conductive substrate for efficient charge transport and good electrolyte penetration, as the TBAPH//Zn cell only exhibits limited capacity (*SI Appendix*, Figure S17). When cycled at the current density of 10 A g^{-1}, an impressive capacity retention of ~80% can be achieved even after 15,000 cycles with the Coulombic efficiency of ~99.6% (Figure 5E). The excellent cycling stability of the TBAPH@GO can be attributed to the unique stabilization process in the first cycle, as the charge-discharge voltage profiles change slowly with the cycle number increases (Figure 5F). It can be further evidenced by the high material stability through *in situ* UV tests using the electrolyte containing 1M $ZnSO_4$ during the 1,000th cycle (*SI Appendix*, Figure S18). Notably, there are no any peaks in the UV spectra representing material dissolution observed at different voltages, suggesting that the TBQPH@GO composite possesses exceptional stability after extended cycling in aqueous environments. Moreover, at a low current density of 0.3 A g^{-1}, a high capacity retention of ~88.2% can be realized after 1000 cycles due to the conjugated molecular structure which facilitates electron delocalization and structural stability (*SI Appendix*, Figure S19). However, the TBQPH//Zn cell exhibited poorer cycling stability and weaker rate performance at 0.3 A g^{-1} over long cycles, clearly demonstrating that the addition of GO enhances the exposure of the material's active surface area and improves both electronic and ionic transport rates (SI Appendix, Figures S20 and S21). We also analyzed the SEM images and XRD patterns of the zinc anode after 1000 cycles. The results show no significant dendrite formation on the electrode before and after cycling, however, basic zinc sulfate was observed on the surface, which may play a critical role in influencing the battery's cycling performance (SI Appendix, Figures S22 and S23). Compared with the state-of-the-art zinc-organic batteries, the TBQPH@GO//Zn battery exhibits simultaneously high rate capability, Coulombic efficiency and cycling stability (Figure 5G).[39-48] We conducted cyclic tests on TBQPH@GO material at a high loading (20 mg/cm²) and found that its capacity contribution approached 70 mAh/g at 0.5 A g^{-1}. (SI Appendix, Figures S24). In terms of specific capacity, working voltage and energy density of organic cathode materials, the TBQPH@GO exhibits an ultrahigh capacity (~445 mAh g^{-1}) as well as a high working voltage (~1.0 V vs. Zn^{2+}/Zn), resulting in a high energy density of ~300 Wh kg^{-1} which is among the best in literature.

Conclusions

In conclusion, this new organic cathode TBQPH with spacer composition of imine groups (C=N) and carbonyl groups (C=O) was designed and synthesized for aqueous zinc ion batteries with high theoretical specific capacity. Theoretical calculations and experimental data demonstrate that the relationship between the conjugated structure, energy gap reduction, electron delocalization enhancement and material stability. Importantly, the combination of TBQPH with GO material enhances its electrochemical performance and stability, exhibiting ultra-high capacity contribution of 445 mAh g^{-1} at a current density of 0.2 A g^{-1} and 200 mAh g^{-1} at a current density of 10 A g^{-1}, while maintaining 80% capacity retention after 15,000 cycles. Calculations and electrochemical tests reveal distinct mechanisms for the first and subsequent cycle reactions in TBQPH, with the imine groups do not participating in the discharge reaction during the initial cycle. The stabilized TBQPH exhibits a stabilization mode of synergistic storage involving carbonyl and imine groups, where the first discharge plateau is attributed to Zn^{2+} insertion while the second and third discharge plateaus are triggered by the co-insertion of Zn^{2+} and H^+. Our work proposes an extended conjugation and "group synergy" approach, which enhances the conductivity, stability, and electrochemical activity of the molecule. Furthermore, this synergistic cation storage mechanism can be extrapolated to the design and application of other n-type molecules. This strategy offers novel insights for designing and developing organic cathode materials for aqueous zinc ion batteries.

Author Contributions

Y.W. and G.Y. directed the project. G.M. and Y.C. for material preparation, characterization and testing, R.W., Z. Y. and H.Y. XPS、XRD、FTIR test and in Raman test were performed, Y.W., H.D., M.C. some constructive suggestions are provided for the experiment. G.M., J.Z. wrote the first draft, and all authors discussed the experimental results and continued to prepare the manuscript.

Conflicts of interest

There are no conflicts to declare.

Acknowledgements

Y.W. acknowledges the support from National Natural Science Foundation of China (61904097). G.Y. acknowledges the support from the Welch Foundation F-1861.

Notes and references

1 Z. Fan, J. Wang, Y. Wu, X. Yan, D. Dai and X.-L. Wu, *J. Energy Chem.* 2024, **97**, 237-264.

2 Y. Fan, Q. Wang, Y. Xie, N. Zhou, Y. Yang, Y. Ding, Y. Wei and G. Qu, *Prog. Mater. Sci.* 2025, **149**, 101393.

3 J. Chen, W. Zhao, J. Jiang, X. Zhao, S. Zheng, Z. Pan and X. Yang, *Energy Storage Mater.* 2023, **59**, 102767.

4 Y. Ou, Y. Xiong, Z. Hu, Y. Zhang and L. Dong, *J. Mater. Chem. A*, 2022, **10**, 10373-10382.

5 F. Hua, Y. Zhang, S. Cao, M. Li, L. Jing and J. Cui, *J. Energy Storage*, 2023, **68**, 107779.

6 K. Yamamoto, D. Suemasa, K. Masuda, K. Aita and T. Endo, *ACS Appl. Mater. Inter.* 2018, **10**, 6346-6353.

7 Z. Song, L. Miao, H. Duan, L. Ruhlmann, Y. Lv, D. Zhu, L. Li, L. Gan and M. Liu, *Angew. Chem. Inter. Edit.* 2022, **61**, e202208821.

8 N. Wang, Z. Guo, Z. Ni, J. Xu, X. Qiu, J. Ma, P. Wei and Y. Wang, *Angew. Chem. Inter. Edit.* 2021, **60**, 20826-20832.

9 D. Li, Y. Guo, C. Zhang, X. Chen, W. Zhang, S. Mei and C.-J. Yao, *Nano-Micro Lett.* 2024, **16**, 194.

10 H.-g. Wang, Q. Wu, L. Cheng and G. Zhu, *Coordin. Chem. Rev.* 2022, **472**, 214772.

11 Z. Li, J. Tan, Y. Wang, C. Gao, Y. Wang, M. Ye and J. Shen, *Energy Environ. Sci.* 2023, **16**, 2398-2431.

12 Y. Gao, J. Yin, X. Xu and Y. Cheng, *J. Mater. Chem. A*, 2022, **10**, 9773-9787.

13 F. Ye, Q. Liu, H. Dong, K. Guan, Z. Chen, N. Ju and L. Hu, *Angew. Chem. Inter. Edit.* 2022, **61**, e202214244.

14 W. Wang, V. S. Kale, Z. Cao, Y. Lei, S. Kandambeth, G. Zou, Y. Zhu, E. Abouhamad, O. Shekhah, L. Cavallo, M. Eddaoudi and H. N. Alshareef, *Adv. Mater.* 2021, **33**, 2103617.

15 X. Geng, H. Ma, F. Lv, K. Yang, J. Ma, Y. Jiang, Q. Liu, D. Chen, Y. Jiang and N. Zhu, *Chem. Eng. J.* 2022, **446**, 137289.

16 J. Kumankuma-Sarpong, S. Tang, W. Guo and Y. Fu, *ACS Appl. Mater. Inter.* 2021, **13**, 4084-4092.

17 D. Ma, H. Zhao, F. Cao, H. Zhao, J. Li, L. Wang and K. Liu, *Chem. Sci.* 2022, **13**, 2385-2390.

18 M. Li, M. Liu, Y. Lu, G. Zhang, Y. Zhang, Z. Li, Q. Xu, H. Liu and Y. Wang, *Adv. Funct. Mater.* 2024, **34**, 2312789.

19 J. Yang, H. Hua, H. Yang, P. Lai, M. Zhang, Z. Lv, Z. Wen, C. C. Li, J. Zhao and Y. Yang, *Adv. Energy Mater.* 2023, **13**, 2204005.

20 D. Kundu, P. Oberholzer, C. Glaros, A. Bouzid, E. Tervoort, A. Pasquarello and M. Niederberger, *Chem. Mater.* 2018, **30**, 3874-3881.

21 Y. Zhang, Q. Huang, Z. Song, L. Miao, Y. Lv, L. Gan, M. Liu,

View Article Online
DOI: 10.1039/D5SC00311C

*Adv. Funct. Mater.*2024, 2416415.
22 N. T. H. Luu, A. S. Ivanov, T.-H. Chen, I. Popovs, J.-C. Lee and W. Kaveevivitchai, *J. Mater. Chem. A*, 2022, **10**, 12371-12377.
23 Z. Song，L. Miao，H. Duan，Y. Lv，L. Gan，M. Liu，*Angew. Chem. Int. Ed.* 2024, **63,** e202401049.
24 X. Deng, J. K. Sarpong, G. Zhang, J. Hao, X. Zhao, L. Li, H. Li, C. Han and B. Li, *InfoMat*, 2023, **5**, e12382.
25 Q. Wang, Y. Liu, C. Wang, X. Xu, W. Zhao, Y. Li and H. Dong, *Chem. Eng. J.* 2023, **451**, 138776.
26 Y. Shi, P. Wang, H. Gao, W. Jin, Y. Chen, Y. Huang, T.-R. Wu, D.-Y. Wu, J. Xu and J. Cao, *Chem. Eng. J.* 2023, **461**, 141850.
27 Y. Gao, G. Li, F. Wang, J. Chu, P. Yu, B. Wang, H. Zhan and Z. Song, *Energy Storage Mater.* 2021, **40**, 31-40.
28 Y. Chen, J. Li, Q. Zhu, K. Fan, Y. Cao, G. Zhang, C. Zhang, Y. Gao, J. Zou, T. Zhai and C. Wang, *Angew. Chem.Inter. Edit.* 2022, **61**, e202116289.
29 H. Peng, J. Xiao, Z. Wu, L. Zhang, Y. Geng, W. Xin, J. Li, Z. Yan, K. Zhang and Z. Zhu, *CCS Chem.* 2022, **5**, 1789-1801.
30 W. Ji, D. Du, J. Liang, G. Li, G. Feng, Z. Yin, J. Zhou, J. Zhao, Y. Shen, H. Huang and S. Pang, *Battery Energy*, 2023, **2**, 20230020.
31 Z. Song，Q. Huang，Y. Lv，L. Gan，M. Liu，*Angew. Chem. Int. Ed.* 2025, **64**, e202418237.
32 W. Sun, M. Ma, M. Zhu, K. Xu, T. Xu, Y. Zhu and Y. Qian, *Small*, 2022, **18**, 2106604.
33 T. Lu and F. Chen, *J. Comput. Chem.*. 2012, **33**, 580-592.
34 T. Zhou, L. Zhu, L. Xie, Q. Han, X. Yang, L. Chen, G. Wang and X. Cao, *J. Coll. Inter. Sci.*2022, **605**, 828-850.
35 G. Li, L. Sun, S. Zhang, C. Zhang, H. Jin, K. Davey, G. Liang, S. Liu, J. Mao and Z. Guo, *Adv. Funct. Mater.* 2024, **34**, 2301291.
36 Y. Wang, C. Wang, Z. Ni, Y. Gu, B. Wang, Z. Guo, Z. Wang, D. Bin, J. Ma and Y. Wang, *Adv. Mater.* 2020, **32**, 2000338.
37 L. Liu, L. Miao, L. Li, F. Li, Y. Lu, Z. Shang and J. Chen, *The J. Phy. Chem. Lett.* 2018, **9**, 3573-3579.
38 J. Murillo-Gelvez, K. P. Hickey, D. M. Di Toro, H. E. Allen, R. F. Carbonaro and P. C. Chiu, *Environ. Sci. Technol.* 2019, **53**, 5816-5827.
39 Q. Zhao, W. Huang, Z. Luo, L. Liu, Y. Lu, Y. Li, L. Li, J. Hu, H. Ma and J. Chen, *Sci. Adv.* **4**, eaao1761.
40 Z. Tie, L. Liu, S. Deng, D. Zhao and Z. Niu, *Angew. Chem. Inter. Edit.* 2020, **59**, 4920-4924.
41 T. Sun, W. Zhang, Q. Nian and Z. Tao, *Chem. Eng. J.* 2023, **452**, 139324.
42 Z. Lin, H.-Y. Shi, L. Lin, X. Yang, W. Wu and X. Sun, *Nature Commun.* 2021, **12**, 4424.
43 K. W. Nam, H. Kim, Y. Beldjoudi, T.-w. Kwon, D. J. Kim and J. F. Stoddart, *J. Am. Chem. Soc.* 2020, **142**, 2541-2548.
44 Q. Wang, Y. Liu and P. Chen, *J. Power Sources*, 2020, **468**, 228401.
45 Q. Wang, X. Xu, G. Yang, Y. Liu and X. Yao, *Chem. Commun.* 2020, **56**, 11859-11862.
46 G. Dawut, Y. Lu, L. Miao and J. Chen, *Inorg. Chem. Front.* 2018, **5**, 1391-1396.
47 T. Sun, Z.-J. Li, Y.-F. Zhi, Y.-J. Huang, H. J. Fan and Q. Zhang, *Adv. Funct. Mater.* 2021, **31**, 2010049.
48 X. Wang, L. Chen, F. Lu, J. Liu, X. Chen and G. Shao, *ChemElectroChem*, 2019, **6**, 3644-3647.

View Article Online
DOI: 10.1039/D5SC00311C

Data Availability Statement

The data supporting this article have been included as part of the Supplementary Information.